

Photocatalytic Reduction of CO₂ with Water into Methanol and Ethanol Using Graphene Derivative–TiO₂ Composites: Effect of pH and Copper(I) Oxide

L. M. Pastrana-Martínez¹ · A. M. T. Silva¹ · N. N. C. Fonseca¹ · J. R. Vaz¹ · J. L. Figueiredo¹ · J. L. Faria¹

Published online: 22 July 2016
© Springer Science+Business Media New York 2016

Abstract Fuels derived from CO₂ can contribute to neutralize the carbon balance in the atmosphere and can be converted into easily transportable liquid chemicals, such as methanol (MeOH) or ethanol (EtOH). In this work, a composite prepared from graphene oxide (GO) and titanium dioxide (TiO₂) is applied to the photocatalytic water reduction of CO₂ into renewable fuels under UV/vis light irradiation. The pH was identified as a key variable towards selective MeOH formation. The prepared GO–TiO₂ composite exhibited superior photocatalytic activity for EtOH production (144.7 μmol g⁻¹ h⁻¹) at pH 11.0 and for MeOH production (47.0 μmol g⁻¹ h⁻¹) at pH 4.0. The effect of copper species in the GO–TiO₂ composite is also assessed and its influence on the photocatalytic reaction inferred. The photocatalysts prepared with copper nitrate as copper precursor exhibited the highest rate of MeOH production at pH 11.0. Accordingly, a conceptual scheme in which the photogenerated electrons are used to reduce CO₂ is proposed.

Keywords CO₂ photoreduction · Methanol · TiO₂ · Graphene oxide · Copper

Electronic supplementary material The online version of this article (doi:10.1007/s11244-016-0655-2) contains supplementary material, which is available to authorized users.

✉ L. M. Pastrana-Martínez
lpastrana@fe.up.pt

¹ Laboratory of Separation and Reaction Engineering – Laboratory of Catalysis and Materials (LSRE-LCM), Faculdade de Engenharia, Universidade do Porto, Rua Dr. Roberto Frias, 4200-465 Porto, Portugal

1 Introduction

Achieving a sustainable, resource-efficient and low-carbon economy is one of the key fundamental challenges for the 21st century [1]. In 2013, the level of global carbon dioxide (CO₂) emissions reached a new record, emissions from fossil-fuel combustion and from industrial processes (production of cement clinker, metals and chemicals) totalling 35.7 billion tonnes CO₂ [2]. This massive release of CO₂ to the atmosphere is believed to result in considerable climate changes, and there are ongoing efforts to reduce its concentration in the atmosphere and to limit its emissions. Different strategies have been used to reduce CO₂ emissions, such as the adsorption of CO₂ into new/functionalized materials, increasing the quantity of green carbon sinks and CO₂ capture followed by compression and geological sequestration, among others [3].

The most obvious reasonable solution is to develop an efficient process for CO₂ conversion into something valuable, but without spilling into the Earth's ecosystems any other chemicals that will damage their functions [4]. One option relies on solar energy, which is an abundant, clean and sustainable resource [5], to photocatalytically convert CO₂ with water into a solar fuel [6–9]. Solar fuels derived from CO₂ can contribute to neutralize the carbon balance in the atmosphere and can be converted into easily transportable liquid chemicals, offering a new opportunity for a sustainable energy supply [10].

Different semiconductors have been applied in the photoreduction of CO₂, TiO₂ being far the most researched photocatalytic material [11–15]. However, practical application of TiO₂ photocatalytic materials is severely compromised by the relatively low visible-light absorption and by the fast electron-hole recombination in the semiconductor material.

A great deal of attention has been recently devoted to the combination of semiconductors with carbonaceous materials, including carbon nanotubes, graphene and graphitic carbon nitride, for the design of high-performance photocatalysts that enhance the photoefficiency of the semiconductors due to the synergistic interaction including both interfacial electron transfer between the two constituent phases and the enhanced adsorption capacity [10, 16–19]. Especially graphene and graphene derivatives in combination with semiconductors have been reported as photocatalysts for CO₂ reduction in the presence of water [10, 15, 20–24]. Overall, the catalytic data show that photocatalysts with very different efficiencies can be obtained by varying the properties of graphene.

The main problem of CO₂ reduction in these systems is that water can compete with CO₂ for capturing the electrons in the conduction band, generating hydrogen and leading to low activity of the photocatalytic CO₂ reduction system [25–31]. One of the most successful strategies to solve this problem consists in the use of a suitable co-catalyst. Some metal nanoparticles can trap electrons from the TiO₂ conduction band, preventing electron-hole recombination and increasing the photocatalytic conversion of CO₂ with water. Among all the reported metals, Pd, Au, Ag and Cu seem to be used most often to increase CO₂ reduction while avoiding hydrogen generation [32–34].

Since both surface modification with metals and the implementation of carbon supports can enhance the rate of CO₂ photoreduction, it is interesting to investigate the synergistic effect of combining the two strategies in a single approach. Furthermore, in an aqueous system, the pH level is a crucial factor, considering its influence on the chemical form of CO₂ dissolved in water, as well as on the respective solubility.

Thus, the aim of the present work is to apply composites prepared from graphene oxide (GO) and titanium dioxide (TiO₂) for the photocatalytic reduction of CO₂ with water into renewable fuels under near-UV/vis irradiation. The effects of initial pH and different precursors of copper as co-catalyst were assessed, and their influence on the photocatalytic reaction inferred. The commercial Evonik TiO₂ catalyst (P25) was used for comparative purposes. Furthermore, a conceptual scheme for CO₂ photoreduction was also proposed to explain the obtained results under UV/vis light irradiation.

2 Materials and Methods

2.1 Chemicals

Ammonium hexafluorotitanate (IV) ((NH₄)₂TiF₆, >99.99 %), boric acid (H₃BO₃, >99 %), ammonium persulfate

((NH₄)₂S₂O₈, >98 %), sulphuric acid (H₂SO₄, >95 %), copper(II) nitrate trihydrate (Cu(NO₃)₂ · 3H₂O, >98 %) and copper(II) acetate (Cu(CH₃COO)₂, 98 %) were obtained from Sigma–Aldrich. Copper(II) chloride (CuCl₂) was purchased from Riedel-de-Haën. Hydrogen peroxide (H₂O₂, 30 % w/w) and sodium hydroxide (NaOH, 98 wt%) were obtained from Panreac, and potassium permanganate (KMnO₄, 99 wt%) from Merck.

The experiments were performed at acidic (4.0), neutral (7.0) and alkaline (11.0) pH. The pH was adjusted by adding HCl 0.1 M or NaOH 0.1 M. The use of a 0.1 mol L⁻¹ sodium carbonate/bicarbonate buffer solution at alkaline conditions helped to maintain the pH of the system, even after bubbling CO₂ into the solution.

2.2 Synthesis of Graphene Oxide (GO) and Graphene Oxide–TiO₂ Composite (GOT)

Graphene oxide was synthesized from synthetic graphite (particle size ≤20 μm, from Sigma–Aldrich) by a modified Hummers method [35, 36] described elsewhere [17]. This method makes use of the Hummers' reagents with additional amounts of NaNO₃ and KMnO₄. The resulting material was dispersed in a given volume of water and sonicated in an ultrasound bath (ultrasonic processor UP400S, 24 kHz) for 1 h. The sonicated dispersion was centrifuged for 30 min at 3000 rpm to remove un-exfoliated graphite oxide particles.

Graphene oxide–TiO₂ (referred as GOT) was prepared by the liquid phase deposition method (LPD) at room temperature as described elsewhere [17]. In this process, ammonium hexafluorotitanate(IV), NH₄TiF₆ (0.1 mol L⁻¹), and boric acid, H₃BO₃ (0.3 mol L⁻¹), were added to the carbon material suspension and heated at 60 °C for 2 h under continuous stirring. The resulting material was washed with water and dried at 100 °C under vacuum for 2 h followed by a post-treatment under N₂ atmosphere at 200 °C. The carbon loading was ca. 4 wt%, taking into account the optimum photocatalytic activity obtained with such composite for the degradation of water organic pollutants in previous works [16, 17, 37]. Bare TiO₂ was also prepared and treated by the same method, without the addition of any carbon material (referred as TiO₂). Degussa P25 from Evonik was used as TiO₂ reference photocatalyst.

2.3 Preparation of Cu-Loaded Catalysts

The Cu-loaded catalysts were prepared by adapting the procedure described by Wu et al. for Cu-loaded TiO₂ [38]. The amount of copper precursor was adjusted to obtain the desired Cu loading of ca. 2 wt%. In detail, Cu(NO₃)₂ · 3H₂O (53.8 mg), Cu(CH₃COO)₂ (40.4 mg) or CuCl₂ (29.9 mg) were directly added during the preparation method of the

catalysts (i.e. TiO_2 or GOT) to obtain 0.8 g of catalyst. The resulting material was separated by filtration, washed with water and dried at 100 °C to remove the adsorbed water overnight. The catalysts were treated in a furnace under air atmosphere heated at 3 °C min^{-1} up to 150 °C for 3 h and then heated at 2 °C min^{-1} up to 500 °C for 5 h. Cu(I) species are predicted to be formed during this calcination step [38]. The composites were labelled as CuCl/GOT, CuAc/GOT and CuN/GOT when respectively using copper chloride, copper acetate or copper nitrate as precursors. The Cu– TiO_2 composites were prepared following the same procedure but without the addition of GO (CuCl/ TiO_2 , CuAc/ TiO_2 and CuN/ TiO_2 , respectively). To compare the catalytic activities, both bare TiO_2 and GOT catalysts were also submitted to a thermal treatment up to 500 °C in air. The samples were denoted as TiO_2 -500 and GOT-500.

2.4 Characterization Techniques

X-ray diffraction (XRD) analysis was performed in a PANalytical X'Pert MPD equipped with an X'Celerator detector and secondary monochromator (Cu $K\alpha$ $\lambda = 0.154$ nm, 50 kV, 40 mA). Rietveld refinement with a PowderCell software was applied for identification of the crystallographic phases. Textural characterization of the materials was obtained from the nitrogen adsorption–desorption isotherms determined at –196 °C in a Quantachrome NOVA 4200e multi-station apparatus. The apparent surface area (S_{BET}) was determined by applying the Brunauer–Emmett–Teller (BET) equation [39].

The point of zero charge (pH_{PZC}) of the materials was determined by preparing solutions with different initial pH (2–10) using 0.1 M HCl or 0.1 M NaOH and 0.01 M of NaCl as electrolyte [16]. Each solution was contacted with 0.15 g of the material and the final pH was measured after 24 h of continuous stirring at 25 °C. The pH_{PZC} value of the material was determined by intercepting the obtained final pH vs. initial pH curve with the straight line final pH = initial pH [40, 41]. The morphology of the composites was studied by scanning electron microscopy (SEM) in a FEI Quanta 400FEG ESEM/EDAX Genesis X4 M instrument. The UV–Vis spectra of the solid powder materials were obtained in a JASCO V-560 UV–Vis spectrophotometer equipped with an integrating sphere attachment (JASCO ISV-469). Barium sulphate was used as the reference. The spectra were recorded in diffuse reflectance mode and transformed by the instrument software to equivalent absorption Kubelka–Munk units. The band gaps of the photocatalysts were determined using the Kubelka–Munk units as a function of the energy.

2.5 Photocatalytic CO_2 Reduction Experiments

The experiments on CO_2 photoreduction with water over the photocatalysts were carried out in a photoreactor system as shown in Fig. 1. The photoreactor was equipped with a UV/vis Heraeus TQ 150 medium-pressure mercury vapor lamp ($\lambda = 254, 313, 365, 436, 546$ and 578 nm) located axially in the reactor and held in a quartz immersion tube with water recirculation to maintain the temperature at around 25 °C. A DURAN 50[®] glass cooling jacket was used for irradiation in the near-UV to visible light range (main resulting emission lines $\lambda = 365, 436, 546$ and 578 nm). In a typical run, the photoreactor was loaded with 250 mL of a solution and 250 mg of catalyst, i.e. a catalyst load of 1 g L^{-1} .

Prior to light irradiation, the described system was degassed with He and CO_2 overnight (10 $\text{cm}^3 \text{min}^{-1}$ and 2 $\text{cm}^3 \text{min}^{-1}$, respectively) to purge air and to saturate the solution. After the purging process, the He and CO_2 flow rates were increased to 27 $\text{cm}^3 \text{min}^{-1}$ and 3 $\text{cm}^3 \text{min}^{-1}$, respectively. The light source was then turned on and the photocatalytic reaction carried out for approximately 3 h under continuous magnetic stirring. To perform the evaluation of the liquid phase reaction products, small aliquots of the suspension were periodically withdrawn by using a syringe, filtered through Millipore membranes (0.45 μm) and then analyzed by gas chromatography (DANI GC-1000) using a capillary column (WCOT Fused Silica 30 m, 0.32 mm i.d., coated with CP-Sil 8 CB low bleed) and a flame ionization detector (FID). The gas phase was monitored by a gas chromatograph (GC) coupled on-line with the reactor and equipped with a thermal conductivity

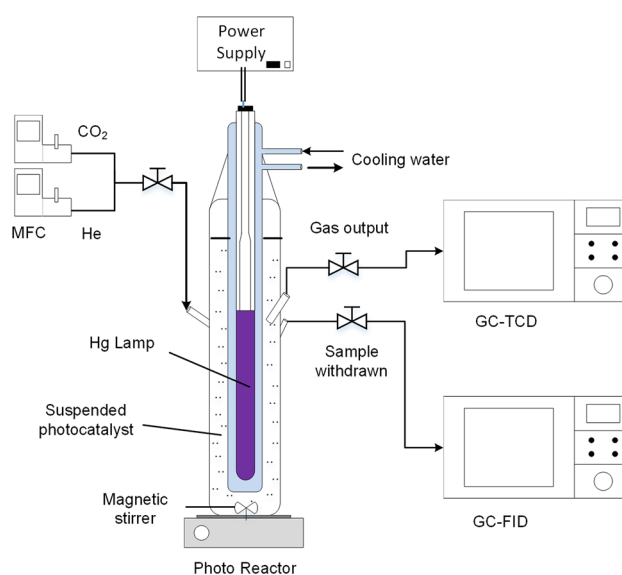


Fig. 1 Experimental set-up for CO_2 photoreduction

detector (TCD), using a capillary column (Carboxen 1010 Plot. Supelco).

3 Results and Discussion

3.1 Catalysts Characterization

The XRD patterns of TiO_2 and Cu-loaded TiO_2 catalysts are shown in Fig. 2a and those obtained for GOT and Cu-loaded GOT catalysts are shown in Fig. 2b. Anatase TiO_2 particles are exclusively formed for all the prepared materials, where the lattice planes of (101) and (004) correspond to the peaks observed at 25.1° and 47.6° , respectively. No obvious carbon diffraction peak for GO was detected in the XRD patterns of GOT and Cu-loaded GOT composites, which could be related to the small amounts of GO in these materials. P25 consists of both anatase and rutile crystalline phases, 80 and 20 %, respectively. The anatase crystallite size was determined by Rietveld refinement using the Williamson–Hall model (Table 1). In this model the crystallite size is calculated from the intercept of the Williamson–Hall plot [42]. The deposition of Cu did not affect the crystalline phase found for both TiO_2 and GOT, although the diffraction peaks of the Cu-loaded catalysts (Fig. 2) were stronger and sharper, in particular for those prepared with TiO_2 , suggesting possible crystallization of some amorphous phase remaining in the catalyst, decrease of lattice defects and/or crystal growth as a consequence of the thermal annealing at 500°C [43]. Peaks related to CuO or Cu_2O were not observed, maybe due to the small copper particles [44, 45].

Nitrogen adsorption isotherms at -196°C were obtained and used in the determination of the specific surface area of the catalyst samples. The N_2 adsorption–desorption isotherms for TiO_2 -based materials and GOT-

based materials are shown in Fig. 3a and b, respectively. The apparent specific surface areas (S_{BET}) of the samples are shown in Table 1. In general, lower surface areas were obtained for the Cu-loaded catalysts compared to both TiO_2 and GOT materials. This effect could be due to the presence of the copper material but also to the treatment with air at 500°C during the preparation step of the copper-loaded materials since bare TiO_2 and GOT were prepared at lower temperature (200°C) under nitrogen atmosphere. It is interesting to note that the surface area of the Cu-loaded GOT photocatalyst prepared with copper nitrate was practically similar to that of the unloaded catalyst ($S_{\text{BET}} = 110$ and $104\text{ m}^2\text{ g}^{-1}$ respectively for GOT and CuN/GOT). GOT and Cu-loaded GOT composites (Fig. 3b) presented larger volume of N_2 adsorbed at high relative pressure and the formation of a hysteresis loop compared to TiO_2 samples, the presence of mesoporosity being evident from the isotherm profile.

Representative SEM images of TiO_2 , GOT composite as well as the copper-loaded photocatalysts are shown in Fig. 4a–h. The morphology of TiO_2 consists of spherical particles that aggregate originating clusters of TiO_2 particles (Fig. 4a). The GOT composite consists of TiO_2 particles aggregated on the GO layers, forming GOT platelets (Fig. 4b) with a uniform TiO_2 distribution on both sides of the graphene oxide sheets [17].

The surface morphology of the Cu-loaded TiO_2 photocatalysts prepared with copper acetate (Fig. 4e) seems similar to that of bare TiO_2 (Fig. 4a). On the contrary, the morphologies observed for both CuCl/TiO_2 and CuN/TiO_2 (Fig. 4c, g, respectively) were different from that obtained for bare TiO_2 , presenting larger clusters. Regarding the Cu-loaded GOT composites (Fig. 4d, f and h), the morphologies obtained were slightly different from that observed for GOT (Fig. 4b), since the platelets were not so notorious when Cu was loaded. All the materials presented quite a

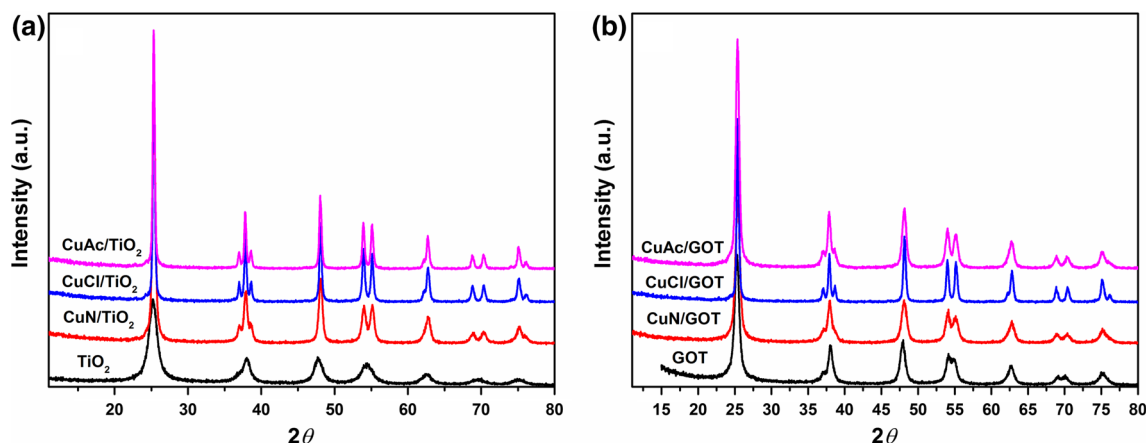
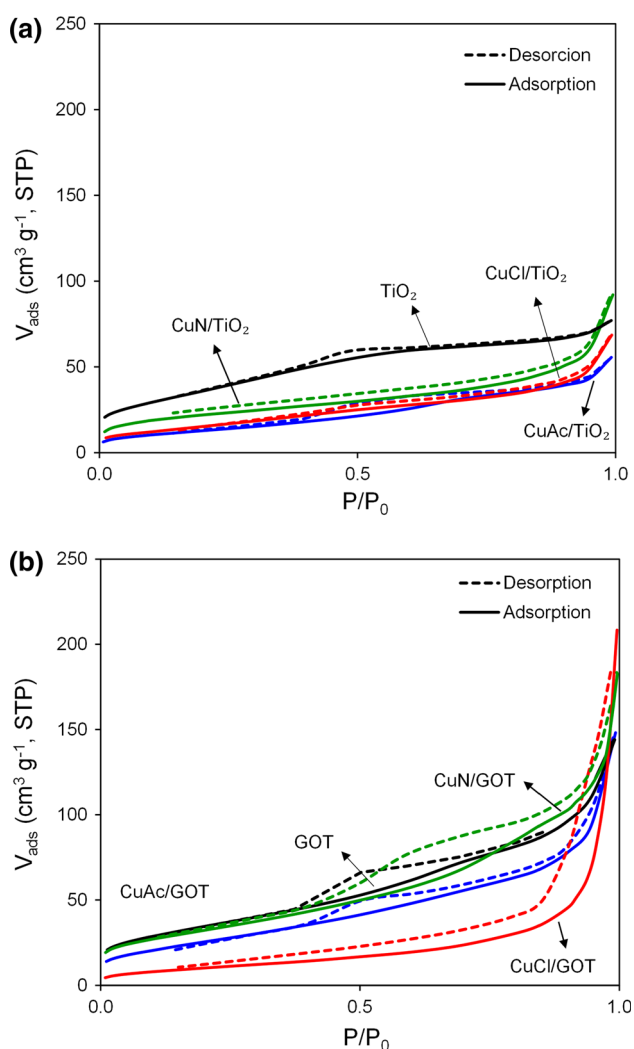


Fig. 2 XRD diffractograms of **a** TiO_2 and Cu-loaded TiO_2 catalysts and **b** GOT and Cu-loaded GOT catalysts

Table 1 BET surface area (S_{BET}), band-gap energy (E_g), pH at the point of zero charge (pH_{PZC}) and copper content obtained from XPS analysis of catalysts

Catalyst	S_{BET} ($\text{m}^2 \text{g}^{-1}$)	E_g (eV)	pH_{PZC}	Crystallite size (nm)	Cu_{XPS} (%)
TiO_2	118	3.12	3.5	8	–
CuCl/TiO_2	54	2.95	3.6	40	~0.5
CuAc/TiO_2	42	3.03	3.8	33	~0.3
CuN/TiO_2	82	2.93	3.8	23	~0.7
GOT	110	2.95	3.2	14	–
CuCl/GOT	30	3.00	3.5	32	~0.5
CuAc/GOT	86	3.10	3.7	20	~0.2
CuN/GOT	104	3.00	3.3	15	~0.6
P25	54	3.20	6.3	22	–

**Fig. 3** N_2 adsorption–desorption isotherms at -196°C of **a** TiO_2 and Cu-loaded TiO_2 catalysts and **b** GOT and Cu-loaded GOT catalysts

homogeneous morphology, but the better assembling of TiO_2 nanoparticles and GO platelets seems to be achieved with GOT. The EDS spectra obtained for the composites (as shown in Fig. 4i for CuN/GOT), revealed Ti, O and C

peaks, that were associated to TiO_2 and to GO (the O peak resulting from TiO_2 and from the oxygenated surface groups present in the chemical structure of GO). It is difficult to infer about the presence of Cu, probably due to the low amounts loaded; nevertheless, there is some indication of the Cu presence in the EDS spectrum (Fig. 4i).

The diffuse reflectance UV/vis spectra of P25 and selected prepared photocatalysts expressed in terms of Kubelka–Munk absorption units, are depicted in Fig. 5. The UV/vis spectra for the samples show the characteristic absorption sharp edge rising at 400 nm, due to the bandgap transition of the TiO_2 semiconductor. P25 exhibited no absorption above its absorption edge, indicating that it will not have photocatalytic response in the visible light region. In contrast, the increase in absorption shown by the GOT composite in the visible spectral range is ascribed to the inherent light absorption capacity of carbon materials and also to the possibility of being photoexcited, in this way promoting electronic transitions between carbon and TiO_2 phases [16, 46]. In general, for all the Cu-loaded catalysts, the band edge is expanded into both UV and visible regions when compared to P25. This effect can be related to the charge transfer transitions between the electrons of the copper co-catalysts and the TiO_2 conduction band [47]. The band gaps for the GOT composite and Cu-loaded materials (Table 1) were lower than for both bare TiO_2 (3.12) and P25 (3.20).

XPS measurements were carried out over the photocatalysts in order to determine the oxidation state of the copper species present in the photocatalysts. As an example, Fig. 6a shows the XPS spectra of the Ti 2p region for both CuN/TiO_2 and CuN/GOT composites. From the Ti 2p region, two peaks were detected and centered at 458.8 and 464.5 eV, corresponding to Ti 2p_{3/2} and Ti 2p_{1/2}, respectively. In addition, the splitting between both peaks was found at 5.7 eV. These results indicate a Ti^{4+} chemical state, typical of TiO_2 as previously reported [17, 48, 49].

The amounts of copper introduced into the surface of the materials were calculated from the XPS data. The photocatalysts prepared with copper nitrate as Cu precursor

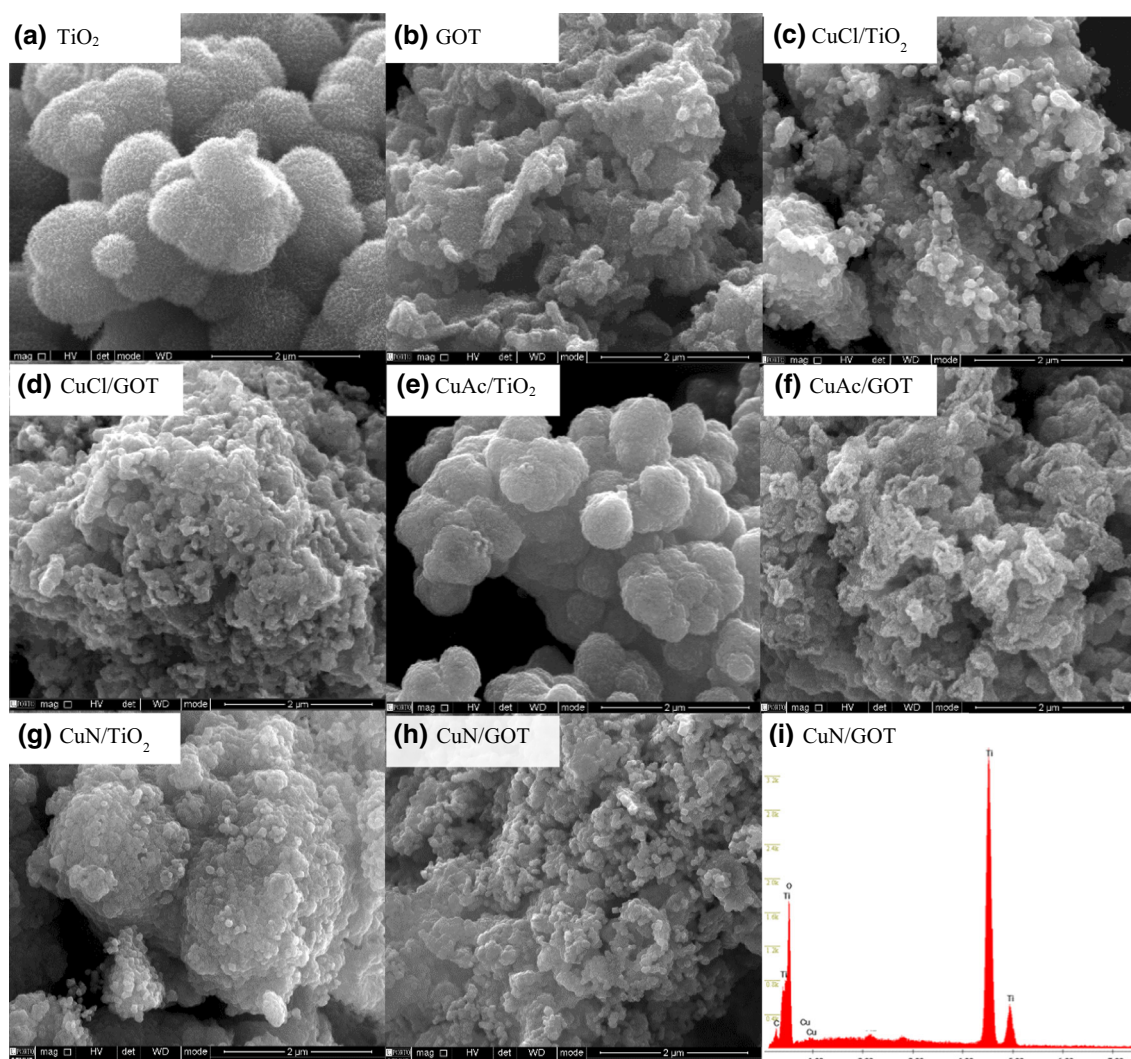


Fig. 4 SEM images of **a** TiO₂, **b** GOT, **c** CuCl/TiO₂, **d** CuCl/GOT, **e** CuAc/TiO₂, **f** CuAc/GOT, **g** CuN/TiO₂, **h** CuN/GOT, **i** EDS spectrum of CuN/GOT

present the largest amount of Cu (0.7 and 0.6 % for CuN/TiO₂ and CuN/GOT, respectively). The low amounts of Cu detected (in comparison with the theoretical 2 wt%) indicate that copper was dispersed mostly inside the structure of the prepared catalysts, rather than at the catalyst surface.

The XPS Cu 2p spectra of the CuN/TiO₂ and CuN/GOT samples are shown in Fig. 6b. The Cu 2p_{3/2} and Cu 2p_{1/2} binding energies of the prepared materials were found to be respectively ca. 932.4 and 952.4 eV, confirming the presence of Cu(I) [50]. It has been reported that, according to the position and the shape of the peaks, the copper on the surface of the catalyst may exist in multiple-oxidation states but Cu(I) is the primary species [51]. These results are in agreement with previous works, where the lower oxidation state of Cu was observed at higher calcination temperatures [38, 48].

3.2 Photocatalytic Reduction Experiments

3.2.1 Effect of Initial pH

In the photocatalytic aqueous system, the pH is an important parameter due to its influence on the chemical form of water dissolved CO₂ and the corresponding solubility. The protonation equilibrium of carbonate ion species depends on the pH (Fig. S1, Supporting Information). At acidic pH (4.0), the predominant carbon species is H₂CO₃. At pH 7.0, HCO₃⁻ ions are the prevalent form (pK_a = 6.4) and at alkaline pH level of 11.0, CO₂ is mainly present in the form of CO₃²⁻ ions (pK_a = 10.3).

The methanol yield (μmol per gram of catalyst) evolution during the photocatalytic experiments for both P25 and GOT at different initial pH (4.0, 7.0 and 11.0) is depicted in Fig. 7a, while the results for ethanol are shown in Fig. 7b.

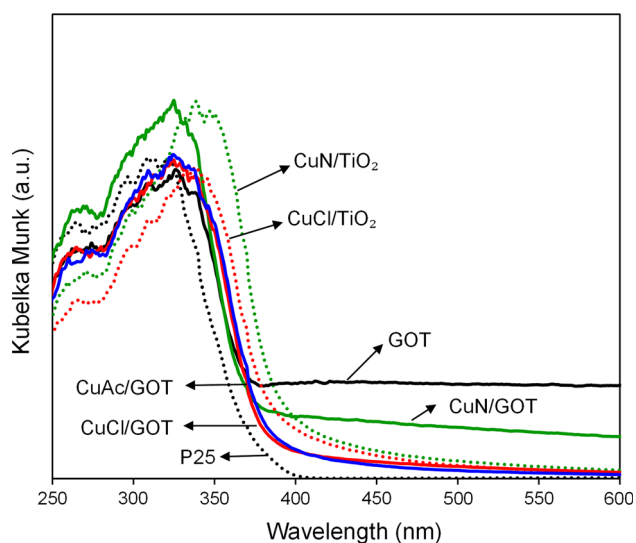


Fig. 5 DRUV-Vis spectra of P25, GOT and some Cu-loaded catalysts

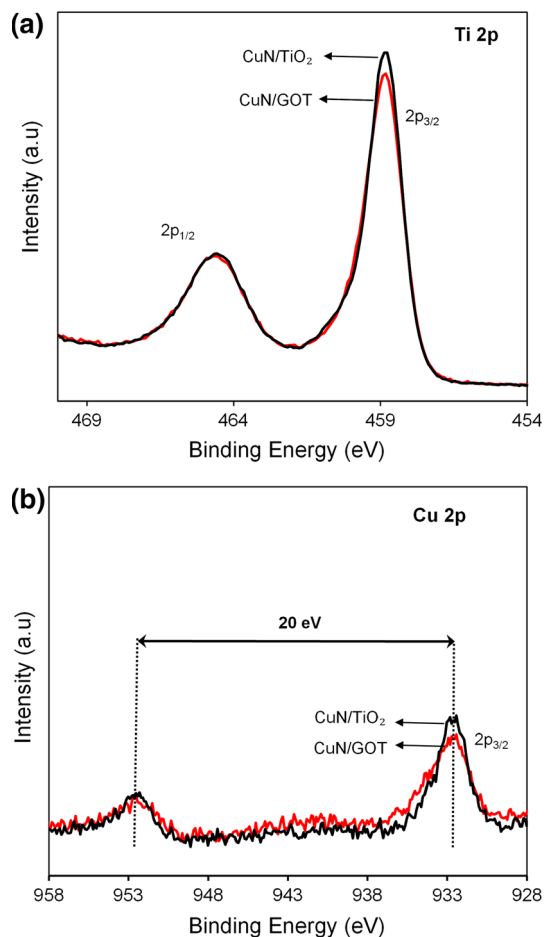


Fig. 6 XPS spectra of the **a** Ti 2p and **b** Cu 2p regions for CuN/TiO₂ and CuN/GOT respectively

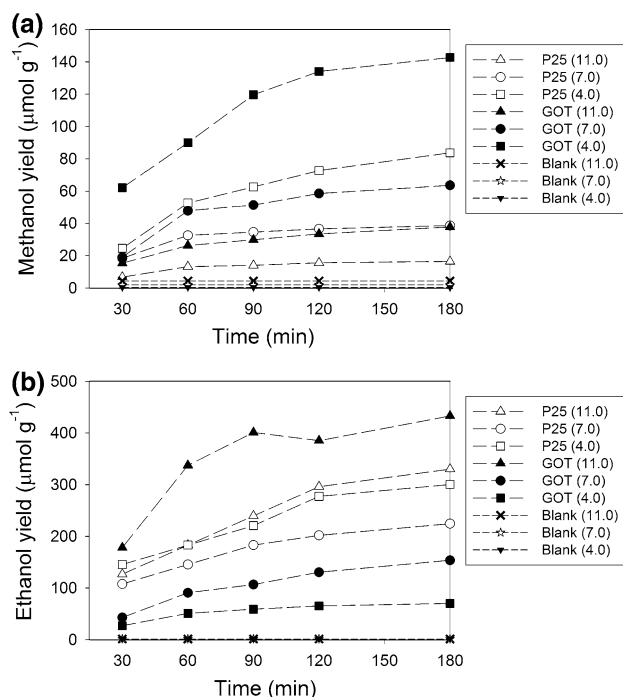


Fig. 7 Methanol **(a)** and ethanol **(b)** yield evolution using P25 and GOT catalysts for different initial solution pH

Photocatalytic experiments were typically carried out during 180 min under near-UV/vis light irradiation. As can be seen, the process is markedly affected by the pH of the initial solution. Both catalysts are able to produce MeOH and EtOH regardless of the pH used, but with different yields. Both methanol and ethanol production strongly increased in the first 60 min of reaction; after that, the increase was less pronounced.

No products were formed in blank tests conducted in the absence of photocatalysts under UV/vis irradiation (Fig. 7), or with catalysts in the dark, indicating that the conversion is a truly photocatalytic reduction process that requires both photocatalysts and UV/vis irradiation. In the photocatalytic process, the main products in the liquid phase were methanol (MeOH) and ethanol (EtOH). No other carbonaceous compounds were observed. In the effluent gas, monitored by GC-TCD, O₂ increased with the irradiation time at the beginning of the reaction, but since the produced O₂ may dissolve in the solution or adsorb on the catalyst surface, it is difficult to determine accurately the amount of O₂. The gas analysis also confirmed that other sub-products such as H₂, CO or CH₄ were not formed during the photoreduction of CO₂, at least in detectable amounts.

The effect of pH on the formation rate of both MeOH and EtOH ($\mu\text{mol g}^{-1} \text{h}^{-1}$) for P25 and GOT photocatalysts at 180 min is shown in Fig. 8a and b, respectively.

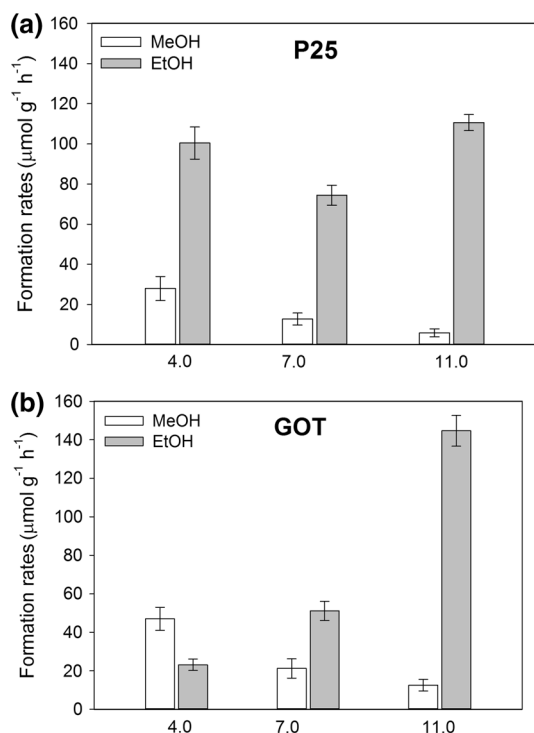
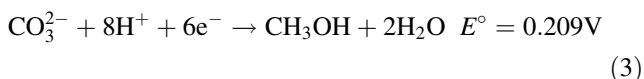
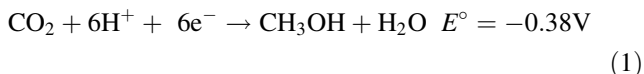


Fig. 8 Methanol and ethanol formation rate at different initial pH for **a** P25 and **b** GOT at 180 min

The MeOH formation rate increased for both P25 and GOT material when the solution pH was decreased from the pH 11.0 (5.8 and $12.5 \mu\text{mol g}^{-1} \text{h}^{-1}$ for P25 and GOT, respectively) to 4.0 (27.9 and $47.0 \mu\text{mol g}^{-1} \text{h}^{-1}$ for P25 and GOT, respectively). This can be explained because low pH favors higher proton concentrations that might decrease the theoretical reduction potential of CO_2 by assisting the electron transfer to CO_2 with protonation of the negative species [15]. In addition, carbonate and bicarbonate species are more difficult to reduce than CO_2 , according to the standard photoreduction potential, E° (Eqs. 1–3) [52]. Moreover, carbonates and bicarbonates are able to act as hole scavengers and may be easily oxidized, inverting the overall process [53]. This effect can be considered negligible in acidic solution, favoring the process at pH 4.0 as previously reported [54].



Regarding EtOH production, Fig. 8a and b show that both catalysts yield the highest performance at pH 11 (110.6 and $144.7 \mu\text{mol g}^{-1} \text{h}^{-1}$ for P25 and GOT, respectively) where the dissolved CO_2 concentration in

water was higher compared to the other pH values. These results indicate that a different predominant mechanism should be involved for each alcohol, since MeOH formation was higher at pH 4.0 and EtOH formation was higher at pH 11.0.

In addition, at pH 4.0, different performances were observed for these catalysts, P25 yielding a high rate of ethanol formation ($100.4 \mu\text{mol g}^{-1} \text{h}^{-1}$), while GOT produced the lowest ethanol formation rate ($23.1 \mu\text{mol g}^{-1} \text{h}^{-1}$). Thus, these results seem to indicate that the optimal pH could be related with the specific catalyst that is employed in this reaction and also with the target product, rather than with the sole effect of the CO_2 amount dissolved into the liquid (increasing with the solution pH). The works reported by Asi et al. [55] and Zhang et al. [56], respectively, referred optima pH of 8.5 with a AgBr/ TiO_2 catalyst and 7 with a graphene- TiO_2 catalyst, regarding the highest yield for MeOH formation. In addition, in the case of the graphene- TiO_2 composite, the results shown in the literature are quite similar at pH 4 and pH 7. Thus, overall, it seems that the process performance strongly depends on the photocatalyst tested and also on other chemical conditions of the reaction medium.

This is in line with the influence of the point of zero charge (PZC) of the employed catalysts (ca. 3.2 for GOT and 6.3 for P25, Table 1). Thus, at pH 4.0, both H_2CO_3 and HCO_3^- are the prevalent carbonate species in solution (Fig. S1, Supporting Information) whereas the surface of P25 is positively charged ($\text{pH}_{\text{PZC}} \approx 6.3$). Therefore, the predominant electrostatic interaction between P25 and bicarbonate species could be responsible for the higher EtOH formation. On the other hand, the surface of the GOT composite ($\text{pH}_{\text{PZC}} \approx 3.2$) is slightly negative and repulsion forces between their negatively charged surfaces and bicarbonate species are expected.

In any case, the results indicate the highest photocatalytic activity for the GOT composite concerning EtOH formation at pH 11.0 and MeOH formation at pH 4.0 (respectively, 144.7 and $47.0 \mu\text{mol g}^{-1} \text{h}^{-1}$). The combination of TiO_2 with GO generates a synergistic effect that potentially enhances the photoactivity due to the possible improvements in the adsorption capacity and efficient interfacial electron transfer between the two constituent phases [17, 18]. In fact, a good assembly and interfacial coupling between the GO sheets and TiO_2 nanoparticles can be observed in the SEM micrograph of this composite (Fig. 4b). Moreover, the combined contribution of the lower band-gap energy (Table 1), as well as the known quenching of photoluminescence determined by Raman spectroscopy for the GOT catalyst [17], could be the possible answer for the higher performance observed when compared with P25, besides possible different mechanisms of reaction. It has also to be considered that strong

adsorption of CO₂ on the GO surface can play a favorable role in the photocatalytic process by increasing the concentration of this substrate near the reactive sites [57, 58].

3.2.2 Effect of Copper Loading

The effect of copper loading on both MeOH and EtOH production during the photocatalytic experiments was investigated at pH 11.0 (Fig. 9a, b, respectively). TiO₂-500 and GOT-500 were used as reference materials. Once again, the yields of both methanol and ethanol had the largest increase during the first 60 min of irradiation time and then the alcohol yield was less noticeable. This observation can be attributed to the re-oxidation of the formed carbon compounds on the photocatalyst surface [59, 60]. Deactivation of copper-loaded catalysts was also probably due to the deposition of poisoning species during the reduction of CO₂ with water [61, 62].

Figure 10 shows the production rates of methanol and ethanol at 180 min under UV–Vis irradiation. It was found that the CO₂ photoreduction of TiO₂-500 slightly increases when thermal annealing was applied at 500 °C due to the growth and improved crystallinity of the TiO₂ nanoparticles, as previously observed by XRD analysis. For the Cu-loaded TiO₂ catalysts (Fig. 10a), the addition of copper to TiO₂ significantly increases the photoactivity towards both

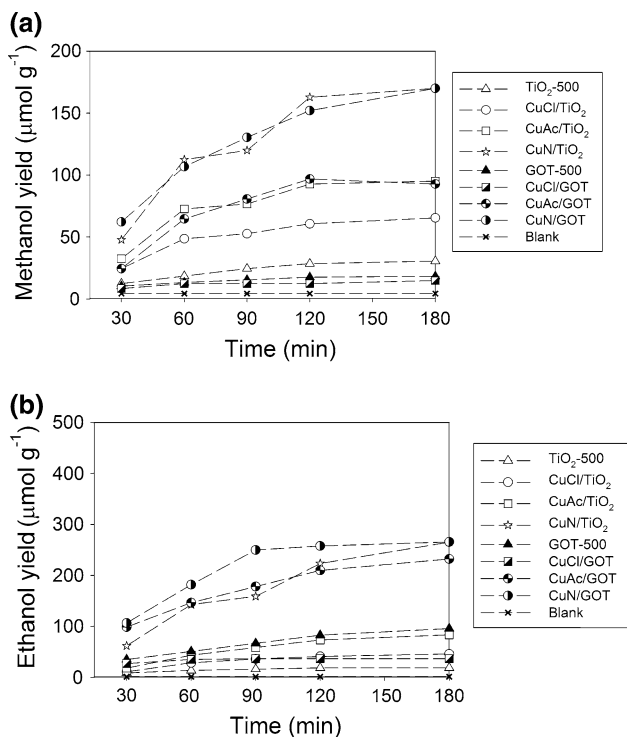


Fig. 9 Methanol (a) and ethanol (b) yield evolution using TiO₂-500, GOT-500 and the Cu-loaded catalysts at pH 11.0

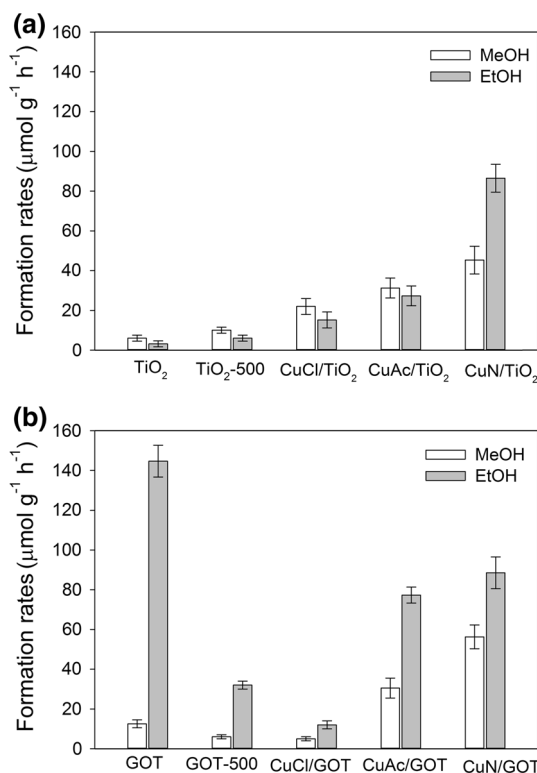


Fig. 10 CO₂ photoreduction over a TiO₂, TiO₂-500 and Cu-loaded TiO₂ catalysts, and b GOT, GOT-500 and Cu-loaded GOT catalysts at initial pH 11.0 and at 180 min

MeOH and EtOH formation. The efficiency of the photocatalytic process depends on the copper precursor used.

The photocatalytic efficiency follows the sequence CuN/TiO₂ > CuAc/TiO₂ > CuCl/TiO₂ > TiO₂-500, the CuN/TiO₂ catalyst presenting a markedly higher activity (45.2 and 86.4 μmol g⁻¹ h⁻¹, for MeOH and EtOH formation rates, respectively) than the other materials tested. This photocatalytic activity may be related with the largest amount of Cu on the surface, in comparison to the other Cu-loaded photocatalysts (derived from the XPS analysis, Table 1). Furthermore, the extended photoresponse range of the CuN/TiO₂ catalyst (Fig. 5) is also expected to provide a positive contribution to the photocatalytic activity.

The results obtained for GOT, GOT-500 and Cu-loaded GOT composites are presented in Fig. 10b. The highest EtOH formation rate was obtained for the pristine GOT catalyst compared to GOT-500 as well as Cu-loaded GOT composites. Thermal treatment at 500 °C results in a marked decrease of activity for the GOT catalyst due to the removal of the oxygenated surface groups of GO, since these groups (such as epoxy and hydroxyl groups) mediate the efficient and uniform assembly of the TiO₂ nanoparticles on the GO sheets as previously reported for the degradation of organic pollutants in aqueous solutions [63].

The presence of Cu increased the alcohol formation rates, especially in the case of MeOH formation, for both CuN/GOT and CuAc/GOT catalysts compared to GOT-500 (respectively 56.2, 30.5 and 6.0 $\mu\text{mol g}^{-1} \text{h}^{-1}$, Fig. 10b). Thus, once again, the highest activity for MeOH production was obtained with the catalysts prepared with copper nitrate as precursor (56.2 $\mu\text{mol g}^{-1} \text{h}^{-1}$ for CuN/GOT). The lowest photocatalytic activity was obtained with CuCl_2 as copper precursor and could be explained by the amount of the inorganic ions (e.g., Cl^-) that may still be present on the catalyst surface even after calcination. These surface contaminants could react with CO_2 and H_2O under light irradiation, interfering with the photoinduced reactions and influencing the photocatalytic activity [25].

On the basis of the above results, a conceptual scheme for the CO_2 photoreduction was proposed, as illustrated in Fig. 11. In this system, p-type Cu_2O , n-type TiO_2 and GO can be connected in the composite forming a p–n heterojunction-like system.

Under UV/vis irradiation, electrons in both Cu_2O and TiO_2 are excited. The very negative potential of the conduction band edge position of Cu_2O ($E_g = 2.0\text{--}2.2 \text{ eV}$) [64] compared to TiO_2 , renders photogenerated electrons with high reducing power. Moreover, it has been proposed that Cu_2O provides sites for the preferential activation and conversion of CO_2 molecules in the presence of H_2O [65]. Thus, the generated carbonate species anchored to the photocatalyst surfaces could efficiently accept the electrons from Cu_2O , resulting in the formation of the CO_2 radical anion ($\text{CO}_2^{\bullet-}$) as previously reported [14, 66, 67]. The $\text{CO}_2^{\bullet-}$ radical anion could react with protons and the hydrogen atoms (H^\bullet , from water reduction) forming methoxyl radicals ($\text{CH}_3\text{O}^\bullet$) and finally methanol ($\text{CH}_3\text{OH} \equiv \text{MeOH}$) after protonation (Fig. 11) [59]. In what concerns the results under alkaline conditions, one possible pathway leading to the major formation of EtOH, in detriment of MeOH, is related to the large number of C1 intermediate

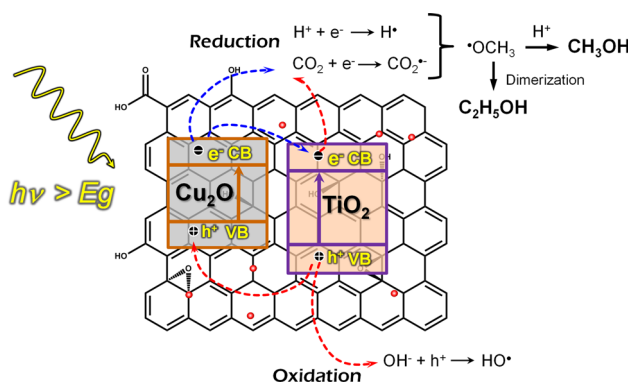


Fig. 11 Conceptual scheme of CO_2 photoreduction catalyzed by Cu-loaded GOT composite

species, derived from CO_2 , that can anchor to the catalyst surface and may cause the dimerization to form EtOH via a radical-substrate reaction mechanism in a H^+ deficient system [68].

Both the conduction and the valence bands of Cu_2O nanoparticles are located above those of TiO_2 as previously reported [69–73]. As Cu_2O is also in contact with TiO_2 , the photogenerated electrons in Cu_2O are able to be directly transferred to TiO_2 for the reduction of CO_2 , leaving the holes on the valence band since the conduction band of Cu_2O is -1.2 eV more negative than that of TiO_2 [74] (Fig. 11). This double pathway for injection of photoelectrons into CO_2 contributes to the enhanced performance of Cu-loaded catalysts to generate MeOH as compared to unmodified catalysts. In addition, the Cu(I) species could constitute the main adsorption sites for CO_2 [75], thereby enhancing the CO_2 reduction rate.

On the other hand, photo-generated holes in the valence band of TiO_2 could oxidize water to produce H^+ and O_2 and they can also migrate to the surface of Cu_2O particles (Fig. 11). The nonexistence of H_2 in the outlet gas suggests that the proton may fail to capture the photogenerated electrons [59].

It is worth noting that the Cu-loaded catalysts change their colour before and after the photocatalytic reaction. The fresh catalysts have a light greenish colour due to the small amount of Cu species. The colour of the catalysts changes to dark grey after the CO_2 photoreduction experiments. It is plausible that Cu_2O species may have suffered a redox cycle where the Cu(I) species can be reduced to Cu(0) metal upon photo-excitation [76]. The composites turned lighter after taking them out from the reactor, i.e., upon exposure to room environment overnight. The change of colour back to light greenish could be due to the re-oxidation of Cu(0) to Cu(I), as previously reported in the literature [33].

Moreover, owing to the excellent electronic conductivity of graphene, the photo-generated electrons could be also transferred to GO, thus promoting charge separation under UV/vis light irradiation.

It appears that the main reason for the high activity and selectivity towards MeOH formation in the Cu-loaded catalysts could be attributed to the plasmon resonance of metallic Cu and the p–n junction $\text{Cu}_2\text{O}/\text{TiO}_2/\text{GO}$, due to the reduction of the recombination of the photoexcited electrons and holes both under UV–Vis irradiation, leading to more effective holes and electrons.

In the field of CO_2 photocatalytic conversion, it is of paramount importance to ensure that the hydrocarbons are formed from the reduction of CO_2 , and not from any possible carbon residues on the catalyst surface or from the carbon materials used in the photocatalysts [77, 78]. In this context, photocatalytic experiments were performed with

the C-containing catalysts (GOT), water and UV/vis light irradiation in the absence of CO₂. The results showed negligible methanol and ethanol yields, confirming that CO₂ is an essential reactant for methanol and ethanol production in the experiments performed as previously reported in the literature [79].

4 Conclusions

The presence of GO and copper in the GOT composites extended the absorption in the visible spectral range, enhancing the CO₂ photoreduction in aqueous phase. The result is the formation of MeOH and EtOH, as main products under near-UV/vis light irradiation. The pH of the aqueous medium was identified as key variable in the product distribution. The synthesized GOT composite revealed high photocatalytic activity for both MeOH and EtOH production at the initial solution pH of 4.0 and 11.0, respectively, exceeding that of the benchmark P25 photocatalyst. This superior performance was attributed to the synergistic interaction encompassing both interfacial electron-transfer between the two constituent phases, as well as to the lower band-gap energy and maybe to the quenching of photoluminescence.

Among all the prepared Cu-loaded composites, CuN/GOT was the best performing material for both MeOH and EtOH production at pH 11.0. In this process, the photo-generated electrons in the p-type Cu₂O semiconductor could reduce CO₂ to the CO₂^{•-} radical anion. Subsequent reaction could involve radical species forming CH₃O• radicals and MeOH after protonation. The formation of EtOH is favored in an H⁺ deficient system, via a radical-substrate reaction mechanism.

Acknowledgments This work was financially supported by Project POCI-01-0145-FEDER-006984—Associate Laboratory LSRE-LCM funded by FEDER through COMPETE2020—Programa Operacional Competitividade e Internacionalização (POCI)—and by national through FCT—Fundação para a Ciência e a Tecnologia. LMPM and AMTS acknowledge the FCT Investigator Programme (IF/01248/2014 and IF/01501/2013, respectively), with financing from the European Social Fund and the Human Potential Operational Programme. Authors are thankful to Dr. Carlos M. Sá (CEMUP) for assistance with XPS analyses.

References

1. Yi Q, Li W, Feng J, Xie K (2015) Carbon cycle in advanced coal chemical engineering. *Chem Soc Rev* 44:5409–5445
2. Olivier J, Janssens-Maenhout G, Muntean M, Peters J (2015) Trends in global CO₂ emissions: 2015 report. PBL Netherlands Environmental Assessment Agency, The Hague, European Commission, Joint Research Centre, Ispra
3. Ahmed N, Shibata Y, Taniguchi T, Izumi Y (2011) Photocatalytic conversion of carbon dioxide into methanol using zinc-copper–M(III) (M = aluminum, gallium) layered double hydroxides. *J Catal* 279:123–135
4. Pérez-Cadenas AF, Ros CH, Morales-Torres S, Pérez-Cadenas M, Kooyman PJ, Moreno-Castilla C, Kapteijn F (2013) Metal-doped carbon xerogels for the electro-catalytic conversion of CO₂ to hydrocarbons. *Carbon* 56:324–331
5. Tran PD, Wong LH, Barber J, Loo JSC (2012) Recent advances in hybrid photocatalysts for solar fuel production. *Energy Environ Sci* 5:5902–5918
6. Ozin GA (2015) Throwing new light on the reduction of CO₂. *Adv Mater* 27:1957–1963
7. Corma A, Garcia H (2013) Photocatalytic reduction of CO₂ for fuel production: possibilities and challenges. *J Catal* 308:168–175
8. Sun P, Zheng F, Zhu M, Song Z, Wang K, Zhong M, Wu D, Little RB, Xu Z, Zhu H (2014) Selective trans-membrane transport of alkali and alkaline earth cations through graphene oxide membranes based on cation–π interactions. *ACS Nano* 8:850–859
9. Perathoner S, Centi G (2014) CO₂ recycling: a key strategy to introduce green energy in the chemical production chain. *ChemSusChem* 7:1274–1282
10. Sun H, Wang S (2014) Research advances in the synthesis of nanocarbon-based photocatalysts and their applications for photocatalytic conversion of carbon dioxide to hydrocarbon fuels. *Energy Fuels* 28:22–36
11. Marszewski M, Cao S, Yu J, Jaroniec M (2015) Semiconductor-based photocatalytic CO₂ conversion. *Mater Horiz* 2:261–278
12. Mao J, Li K, Peng T (2013) Recent advances in the photocatalytic CO₂ reduction over semiconductors. *Catal Sci Technol* 3:2481–2498
13. Ola O, Maroto-Valer MM (2015) Review of material design and reactor engineering on TiO₂ photocatalysis for CO₂ reduction. *J Photochem Photobiol C* 24:16–42
14. Habisreutinger SN, Schmidt-Mende L, Stolarczyk JK (2013) Photocatalytic reduction of CO₂ on TiO₂ and other semiconductors. *Angew Chem Int Ed* 52:7372–7408
15. Dhakshinamoorthy A, Navalon S, Corma A, Garcia H (2012) Photocatalytic CO₂ reduction by TiO₂ and related titanium containing solids. *Energy Environ Sci* 5:9217–9233
16. Pastrana-Martínez LM, Morales-Torres S, Papageorgiou SK, Katsaros FK, Romanos GE, Figueiredo JL, Faria JL, Falaras P, Silva AMT (2013) Photocatalytic behaviour of nanocarbon–TiO₂ composites and immobilization into hollow fibres. *Appl Catal B* 142–143:101–111
17. Pastrana-Martínez LM, Morales-Torres S, Likodimos V, Figueiredo JL, Faria JL, Falaras P, Silva AMT (2012) Advanced nanostructured photocatalysts based on reduced graphene oxide–TiO₂ composites for degradation of diphenhydramine pharmaceutical and methyl orange dye. *Appl Catal B* 123–124:241–256
18. Morales-Torres S, Pastrana-Martínez LM, Figueiredo JL, Faria JL, Silva AMT (2012) Design of graphene-based TiO₂ photocatalysts—a review. *Environ Sci Pollut Res* 19:3676–3687
19. Zheng Y, Liu J, Liang J, Jaroniec M, Qiao SZ (2012) Graphitic carbon nitride materials: controllable synthesis and applications in fuel cells and photocatalysis. *Energy Environ Sci* 5:6717–6731
20. Tu W, Zhou Y, Liu Q, Tian Z, Gao J, Chen X, Zhang H, Liu J, Zou Z (2012) Robust hollow spheres consisting of alternating titania nanosheets and graphene nanosheets with high photocatalytic activity for CO₂ conversion into renewable fuels. *Adv Funct Mater* 22:1215–1221
21. Yu J, Jin J, Cheng B, Jaroniec M (2014) A noble metal-free reduced graphene oxide–CdS nanorod composite for the enhanced visible-light photocatalytic reduction of CO₂ to solar fuel. *J Mater Chem A* 2:3407–3416

22. Fotiou T, Triantis TM, Kaloudis T, Pastrana-Martínez LM, Likodimos V, Falaras P, Silva AMT, Hiskia A (2013) Photocatalytic degradation of microcystin-LR and off-odor compounds in water under UV-A and solar light with a nanostructured photocatalyst based on reduced graphene oxide–TiO₂ composite. identification of intermediate products. *Ind Eng Chem Res* 52:13991–14000
23. Wang P-Q, Bai Y, Luo P-Y, Liu J-Y (2013) Graphene-WO₃ nanobelit composite: elevated conduction band toward photocatalytic reduction of CO₂ into hydrocarbon fuels. *Catal Commun* 38:82–85
24. Kumar P, Mungse HP, Cordier S, Boukherroub R, Khatri OP, Jain SL (2015) Hexamolybdenum clusters supported on graphene oxide: visible-light induced photocatalytic reduction of carbon dioxide into methanol. *Carbon* 94:91–100
25. Wang W-N, Soulis J, Yang YJ, Biswas P (2014) Comparison of CO₂ photoreduction systems: a review. *Aerosol Air Qual Res* 14:533–549
26. Tu W, Zhou Y, Zou Z (2014) Photocatalytic conversion of CO₂ into renewable hydrocarbon fuels: state-of-the-art accomplishment, challenges, and prospects. *Adv Mater* 26:4607–4626
27. Slamet Hosna W, Nasution Ezza Purnama, Riyani Kapti, Gunlazuardi J (2009) Effect of copper species in a photocatalytic synthesis of methanol from carbon dioxide over copper-doped titania catalysts. *World Appl Sci J* 6:112–122
28. Slamet Nasution HW, Purnama E, Kosela S, Gunlazuardi J (2005) Photocatalytic reduction of CO₂ on copper-doped Titania catalysts prepared by improved-impregnation method. *Catal Commun* 6:313–319
29. Kočí K, Matějů K, Obalová L, Krejčíková S, Lacný Z, Plachá D, Čapek L, Hospodková A, Šolcová O (2010) Effect of silver doping on the TiO₂ for photocatalytic reduction of CO₂. *Appl Catal B* 96:239–244
30. Liu E, Kang L, Wu F, Sun T, Hu X, Yang Y, Liu H, Fan J (2014) Photocatalytic reduction of CO₂ into methanol over Ag/TiO₂ nanocomposites enhanced by surface plasmon resonance. *Plasmonics* 9:61–70
31. Truong QD, Liu J-Y, Chung C-C, Ling Y-C (2012) Photocatalytic reduction of CO₂ on FeTiO₃/TiO₂ photocatalyst. *Catal Commun* 19:85–89
32. Zhang Q-H, Han W-D, Hong Y-J, Yu J-G (2009) Photocatalytic reduction of CO₂ with H₂O on Pt-loaded TiO₂ catalyst. *Catal Today* 148:335–340
33. Li Y, Wang W-N, Zhan Z, Woo M-H, Wu C-Y, Biswas P (2010) Photocatalytic reduction of CO₂ with H₂O on mesoporous silica supported Cu/TiO₂ catalysts. *Appl Catal B* 100:386–392
34. Ishitani Osamu, Inoue C, Suzuki Y, Ibusuki T (1993) Photocatalytic reduction of carbon dioxide to methane and acetic acid by an aqueous suspension of metal-deposited TiO₂. *J Photochem Photobiol A* 72:269–271
35. Hummers WS, Offeman RE (1958) Preparation of graphitic oxide. *J Am Chem Soc* 80:1339–1339
36. Stankovich S, Dikin DA, Piner RD, Kohlhaas KA, Kleinhammes A, Jia Y, Wu Y, Nguyen ST, Ruoff RS (2007) Synthesis of graphene-based nanosheets via chemical reduction of exfoliated graphite oxide. *Carbon* 45:1558–1565
37. Pastrana-Martínez LM, Morales-Torres S, Carabineiro SAC, Buijnsters JG, Faria JL, Figueiredo JL, Silva AMT (2013) Nanodiamond–TiO₂ composites for heterogeneous photocatalysis. *Chempluschem* 78:801–807
38. Wu JCS, Lin H-M (2005) Photo reduction of CO₂ to methanol via TiO₂ photocatalyst. *Int J Photoenergy* 7:115–119
39. Brunauer S, Emmett PH, Teller E (1938) Adsorption of gases in multimolecular layers. *J Am Chem Soc* 60:309–319
40. Ferro-García MA, Rivera-Utrilla J, Bautista-Toledo I, Moreno-Castilla C (1998) Adsorption of humic substances on activated carbon from aqueous solutions and their effect on the removal of Cr(III) Ions. *Langmuir* 14:1880–1886
41. Rivera-Utrilla J, Bautista-Toledo I, Ferro-García MA, Moreno-Castilla C (2001) Activated carbon surface modifications by adsorption of bacteria and their effect on aqueous lead adsorption. *J Chem Technol Biotechnol* 76:1209–1215
42. Khorsand Zak A, Abd. Majid WH, Abrishami ME, Yousefi R (2011) X-ray analysis of ZnO nanoparticles by Williamson-Hall and size-strain plot methods. *Solid State Sci* 13:251–256
43. Gonell F, Puga AV, Julián-López B, García H, Corma A (2016) Copper-doped titania photocatalysts for simultaneous reduction of CO₂ and production of H₂ from aqueous sulfide. *Appl Catal B* 180:263–270
44. Navas J, Sanchez-Coronilla A, Aguilar T, Hernandez NC, de los Santos DM, Sanchez-Marquez J, Zorrilla D, Fernandez-Lorenzo C, Alcantara R, Martin-Calleja J (2014) Experimental and theoretical study of the electronic properties of Cu-doped anatase TiO₂. *Phys Chem Chem Phys* 16:3835–3845
45. Xin B, Wang P, Ding D, Liu J, Ren Z, Fu H (2008) Effect of surface species on Cu–TiO₂ photocatalytic activity. *Appl Surf Sci* 254:2569–2574
46. Silva CG, Faria JL (2010) Photocatalytic oxidation of benzene derivatives in aqueous suspensions: synergic effect induced by the introduction of carbon nanotubes in a TiO₂ matrix. *Appl Catal B* 101:81–89
47. Wang C, Chen Z, Jin H, Cao C, Li J, Mi Z (2014) Enhancing visible-light photoelectrochemical water splitting through transition-metal doped TiO₂ nanorod arrays. *J Mater Chem A* 2:17820–17827
48. Lalitha K, Sadanandam G, Kumari VD, Subrahmanyam M, Sreedhar B, Hebalkar NY (2010) Highly stabilized and finely dispersed Cu₂O/TiO₂: a promising visible sensitive photocatalyst for continuous production of hydrogen from glycerol: water mixtures. *J Phys Chem C* 114:22181–22189
49. Sampaio MJ, Pastrana-Martínez LM, Silva AMT, Buijnsters JG, Han C, Silva CG, Carabineiro SAC, Dionysiou DD, Faria JL (2015) Nanodiamond–TiO₂ composites for photocatalytic degradation of microcystin-LA in aqueous solutions under simulated solar light. *RSC Adv* 5:58363–58370
50. Ghijzen J, Tjeng LH, van Elp J, Eskes H, Westerink J, Sawatzky GA, Czyzyk MT (1988) Electronic structure of Cu₂O and CuO. *Phys Rev B: Condens Matter* 38:11322–11330
51. Tseng IH, Wu JCS, Chou H-Y (2004) Effects of sol–gel procedures on the photocatalysis of Cu/TiO₂ in CO₂ photoreduction. *J Catal* 221:432–440
52. Tahir M, Amin NS (2013) Recycling of carbon dioxide to renewable fuels by photocatalysis: prospects and challenges. *Renew Sustain Energy Rev* 25:560–579
53. Neațu Ș, Maciá-Agulló JA, Concepción P, Garcia H (2014) Gold-copper nanoalloys supported on TiO₂ as photocatalysts for CO₂ reduction by water. *J Am Chem Soc* 136:15969–15976
54. Yang X, Xiao T, Edwards PP (2011) The use of products from CO₂ photoreduction for improvement of hydrogen evolution in water splitting. *Int J Hydrogen Energy* 36:6546–6552
55. Abou Asi M, He C, Su M, Xia D, Lin L, Deng H, Xiong Y, Qiu R, X-z Li (2011) Photocatalytic reduction of CO₂ to hydrocarbons using AgBr/TiO₂ nanocomposites under visible light. *Catal Today* 175:256–263
56. Zhang Q, Lin C-F, Chen B-Y, Ouyang T, Chang C-T (2015) Deciphering visible light photoreductive conversion of CO₂ to formic acid and methanol using waste prepared material. *Environ Sci Technol* 49:2405–2417
57. Ghosh A, Subrahmanyam KS, Krishna KS, Datta S, Govindaraj A, Pati SK, Rao CNR (2008) Uptake of H₂ and CO₂ by graphene. *J Phys Chem C* 112:15704–15707
58. Huang B, Li Z, Liu Z, Zhou G, Hao S, Wu J, Gu B-L, Duan W (2008) Adsorption of gas molecules on graphene nanoribbons and

- its implication for nanoscale molecule sensor. *J Phys Chem C* 112:13442–13446
59. Mao J, Peng T, Zhang X, Li K, Ye L, Zan L (2013) Effect of graphitic carbon nitride microstructures on the activity and selectivity of photocatalytic CO₂ reduction under visible light. *Catal Sci Technol* 3:1253–1260
60. Ola O, Maroto-Valer M, Liu D, Mackintosh S, Lee C-W, Wu JCS (2012) Performance comparison of CO₂ conversion in slurry and monolith photoreactors using Pd and Rh-TiO₂ catalyst under ultraviolet irradiation. *Appl Catal B* 126:172–179
61. Kyriacou G, Anagnostopoulos A (1992) An international journal devoted to all aspects of electrode kinetics, interfacial structure, properties of electrolytes, colloid and biological electrochemistry electrochemical reduction of CO₂ at Cu + Au electrodes. *J Electroanal Chem* 328:233–243
62. Smith BD, Irish DE, Kedzierzawski P, Augustynski J (1997) A surface enhanced raman scattering study of the intermediate and poisoning species formed during the electrochemical reduction of CO₂ on copper. *J Electrochem Soc* 144:4288–4296
63. Pastrana-Martínez LM, Morales-Torres S, Likodimos V, Falaras P, Figueiredo JL, Faria JL, Silva AMT (2014) Role of oxygen functionalities on the synthesis of photocatalytically active graphene–TiO₂ composites. *Appl Catal B* 158–159:329–340
64. Nakaoka K, Ueyama J, Ogura K (2004) Photoelectrochemical behavior of electrodeposited CuO and Cu₂O thin films on conducting substrates. *J Electrochem Soc* 151:C661–C665
65. Zhai Q, Xie S, Fan W, Zhang Q, Wang Y, Deng W, Wang Y (2013) Photocatalytic conversion of carbon dioxide with water into methane: platinum and copper(I) oxide co-catalysts with a core-shell structure. *Angew Chem Int Ed* 52:5776–5779
66. Dimitrijevic NM, Vijayan BK, Poluektov OG, Rajh T, Gray KA, He H, Zapol P (2011) Role of water and carbonates in photocatalytic transformation of CO₂ to CH₄ on titania. *J Am Chem Soc* 133:3964–3971
67. Anpo M, Chiba K (1992) Photocatalytic reduction of CO₂ on anchored titanium oxide catalysts. *J Mol Catal* 74:207–212
68. Paul J, Hoffmann FM (1988) CO₂ conversion and oxalate stability on alkali promoted metal surfaces: sodium modified Al(100). *Catal Lett* 1:445–455
69. Hou Y, Li X, Zou X, Quan X, Chen G (2009) Photoelectrocatalytic activity of a Cu₂O-loaded self-organized highly oriented TiO₂ nanotube array electrode for 4-chlorophenol degradation. *Environ Sci Technol* 43:858–863
70. Paracchino A, Laporte V, Sivula K, Grätzel M, Thimsen E (2011) Highly active oxide photocathode for photoelectrochemical water reduction. *Nat Mater* 10:456–461
71. Zhang J, Zhu H, Zheng S, Pan F, Wang T (2009) TiO₂ film/Cu₂O microgrid heterojunction with photocatalytic activity under solar light irradiation. *ACS Appl Mater Interfaces* 1:2111–2114
72. Luo Z, Jiang H, Li D, Hu L, Geng W, Wei P, Ouyang P (2014) Improved photocatalytic activity and mechanism of Cu₂O/N-TiO₂ prepared by a two-step method. *RSC Adv* 4:17797–17804
73. Sun M, Fang Y, Wang Y, Sun S, He J, Yan Z (2015) Synthesis of Cu₂O/graphene/rutile TiO₂ nanorod ternary composites with enhanced photocatalytic activity. *J Alloy Compd* 650:520–527
74. Morales J, Espinos JP, Caballero A, Gonzalez-Elipse AR, Mejias JA (2005) XPS study of interface and ligand effects in supported Cu₂O and CuO nanometric particles. *J Phys Chem B* 109:7758–7765
75. Kakumoto T (1995) A theoretical study for the CO₂ hydrogenation mechanism on Cu/ZnO catalyst. *Energy Convers Manag* 36:661–664
76. Sinatra L, LaGrow AP, Peng W, Kirmani AR, Amassian A, Idriss H, Bakr OM (2015) A Au/Cu₂O-TiO₂ system for photo-catalytic hydrogen production. A pn-junction effect or a simple case of in situ reduction? *J Catal* 322:109–117
77. Izumi Y (2013) Recent advances in the photocatalytic conversion of carbon dioxide to fuels with water and/or hydrogen using solar energy and beyond. *Coord Chem Rev* 257:171–186
78. Yang C-C, Yu Y-H, van der Linden B, Wu JCS, Mul G (2010) Artificial photosynthesis over crystalline TiO₂-based catalysts: fact or fiction? *J Am Chem Soc* 132:8398–8406
79. Liu D, Fernández Y, Ola O, Mackintosh S, Maroto-Valer M, Parlett CMA, Lee AF, Wu JCS (2012) On the impact of Cu dispersion on CO₂ photoreduction over Cu/TiO₂. *Catal Commun* 25:78–82